

AutoAtlas: Neural Network for 3D Unsupervised Partitioning and Representation Learning

K. Aditya Mohan[✉], *Senior Member, IEEE*, Alan D. Kaplan[✉], *Member, IEEE*

Abstract—We present a novel neural network architecture called AutoAtlas for fully unsupervised partitioning and representation learning of 3D brain Magnetic Resonance Imaging (MRI) volumes. AutoAtlas consists of two neural network components: one neural network to perform multi-label partitioning based on local texture in the volume, and a second neural network to compress the information contained within each partition. We train both of these components simultaneously by optimizing a loss function that is designed to promote accurate reconstruction of each partition, while encouraging spatially smooth and contiguous partitioning, and discouraging relatively small partitions. We show that the partitions adapt to the subject specific structural variations of brain tissue while consistently appearing at similar spatial locations across subjects. AutoAtlas also produces very low dimensional features that represent local texture of each partition. We demonstrate prediction of metadata associated with each subject using the derived feature representations and compare the results to prediction using features derived from FreeSurfer anatomical parcellation. Since our features are intrinsically linked to distinct partitions, we can then map values of interest, such as partition-specific feature importance scores onto the brain for visualization.

Index Terms—Brain Imaging, MRI, Representation Learning, Deep Learning, CNN.

I. INTRODUCTION

Representation learning is an important task in data analysis and machine learning. The goal of representation learning is to find a compressed, lower dimensional version of the data that is suitable for a particular task, such as prediction or pattern discovery [1]. Common examples include Principal Component Analysis (PCA), nonlinear kernel representation, and autoencoders (as computed by Neural Networks), see e.g. [2]–[4]. In addition, it is often desired to compute representations that contain meaningful semantic interpretation for the specific applications. In natural images, this could include features, or dimensions, in the representation that correspond to elements such as pose, background, or lighting conditions (see e.g. [5], [6]).

A. Representation Learning for Volumes

A particularly difficult challenge is performing representation learning for 3-dimensional (3D) volumes, such as Magnetic Resonance Imaging (MRI) brain images. First is the challenge of scale and resulting complexity of 3-dimensional data.

K. A. Mohan is with the Computational Engineering Division (CED) at Lawrence Livermore National Laboratory, Livermore, CA, 94551 USA. E-mail: mohan3@llnl.gov, adityakadri@gmail.com.

A. D. Kaplan is with the Computational Engineering Division (CED) at Lawrence Livermore National Laboratory, Livermore, CA, 94551 USA. E-mail: kaplan7@llnl.gov.

We also include supporting files in the form of videos.

Treating 3D data as a series of 2D slices is often undesired, since a particular choice of spatial slice orientation is arbitrary. Secondly, for medical imagery such as MRI, we are often concerned about spatially localizing the derived representation. A representation that maintains the 3D organization and is spatially sensitive would enable a common vocabulary of the representation across individuals (e.g. features related to the same tissue type such as bone can then be compared).

The brain as a complex organ adds another difficult challenge because of its detailed anatomical organization. With respect to tissue structure, the brain contains cortical gray matter, white matter, subcortical gray matter, and the ventricles. We exclude the bone of the skull in this list because tools exist to extract the brain from the skull within MRI. Beyond the tissue types, regions of the cortical and subcortical gray matter are known to be tuned to specific functional tasks, for example, related to performing motor or visual tasks [7]. Indeed, the interplay between the spatial organization of the brain and its function is a central theme in neuroscience, where it is known that the anatomical regions in the brain perform distinct tasks [8]. Because of this, invariance to spatial location of learned image features may be an undesired effect for representation learning of brain imagery. All of this organization can be incorporated in representations computed from MRI. One key challenge, therefore, is the construction of representations which are sensitive to the spatial layout of the brain.

In this paper, we present AutoAtlas, which is a data-driven and fully unsupervised approach for constructing representations of volumetric imagery that simultaneously performs partitioning of the volume and feature extraction of each partition. This is accomplished by encouraging the representation to adhere to spatial constraints in the loss function. The result is a novel approach to representation learning for 3D volumes that directly associates spatial partitions with learned representations, and we demonstrate the utility of this approach in an empirical prediction task. We utilize data from the Human Connectome Project to train the models, which has released a dataset of healthy young adults (HCP-YA) that includes approximately 1,200 subjects along with static measures such as prior health history, emotional processing, cognitive performance, and motor skills [9]–[13]. We use the output of the minimal processing pipeline as specified by the HCP-YA documentation [14]. For this work, we utilized T1 MRI volumes in native volume space. An IRB exemption was obtained through the LLNL Institutional Review Board for use of the HCP-YA data.

AutoAtlas simultaneously learns partitions that correspond across subjects and features associated with each partition.

This is accomplished by a connected pair of neural network architectures: one that predicts partition labels in the input volume, and another that compresses the information within each partition. The approach does not require any manual labeling or secondary partitioning of the volumes and therefore operates in a fully unsupervised setting. We show examples of the resulting partitions and quantify its stability across patients by anchoring to tissue segmentations.

B. Prediction Using MRI

Data-driven analysis and machine learning has shown promise in finding associations between brain imagery and predictive targets [15], [16]. These approaches rely on large collections of imagery and are trained to predict disease states or behavioral characteristics. This type of prediction using brain imagery is an important problem in computational neuroscience with broad applications in clinical and scientific domains [15]. The advantage of separating representation learning and prediction is of special importance to many applications that require multiple predictions because the generation of distinct representations for each separate predictive task obstructs spatially derived insights that may be present across predictive tasks.

The novel contributions of this paper are as follows -

- Neural network architecture called AutoAtlas for fully unsupervised data-driven partitioning and representation learning of 3D volumes without the use of any prior knowledge.
- Loss function called Neighborhood Label Similarity (NLS) loss that encourages AutoAtlas to produce partitions where each voxel is forced to predict a single partition label with high confidence. The NLS loss is also responsible for producing smooth and contiguous partitions.
- Loss function called Anti-Devouring (AD) loss which encourages a pre-defined minimum number of voxels to predict each partition.
- Representation learning using AutoAtlas' features that are uniquely associated with each partition.

We evaluate the predictive performance of AutoAtlas' features for several measures included in the HCP-YA dataset [9]–[14] using several regressors, including linear regression, support vector machine, multilayer perceptron, and nearest neighbor methods. We compare the performance using AutoAtlas features and features associated with established anatomical regions as produced by Freesurfer [17] that is included in the HCP-YA dataset. Using the prediction results, we then compute importance scores for each partition and map them back onto the input brain volumes, to show partitions that are more important for the given prediction task. We have publicly released the code for AutoAtlas under an open-source license at <https://github.com/LLNL/autoatlas>.

II. RELATED WORK

This work is related to several areas that intersect brain imaging and computer vision.

Segmentation and Landmark Collocation: Supervised techniques for semantic segmentation include fully Convolutional Neural Networks (CNNs) [18], and the U-net architecture, which was developed initially for medical image segmentation [19], [20]. Unsupervised techniques for image segmentation are much more difficult in part because of the lack of objective performance criteria. An unsupervised, but not data-driven, approach for medical imagery (e.g. Computed Tomography or abdominal MRI) has been developed [21]. However, as opposed to this method, the collocation of landmarks in images within an unsupervised framework is of interest in the present work [22]–[26]. In particular, our work is motivated by a novel approach for collocation of facial landmarks [27]. In that work, a dual landmark detection and representation learning approach was taken to localize the salient landmarks. In our work, we adopt a similar concept for 3D volumes instead of 2D images, and broaden the landmarks to 3D regions in the volume. This necessitates the development of a novel loss function to encourage well-behaved regions. We refer to the resulting 3D regions as *partitions* rather than segments (and the process as *partitioning* rather than segmenting) since our application differs from classical problems of segmentation in computer vision.

Anatomical Neuroimaging Based Parcellation: A host of atlases have been produced that subdivide the brain into physiologically relevant regions [28]. The method for segmentation varies from registration onto a fixed reference brain to semi-supervised areal classifier [17], [29], [30]. Many approaches for data-driven prediction of anatomical regions utilize datasets of manually labeled regions [31]–[34]. Methodologies also exist for segmentation of brain images containing pathologies [35], [36]. Unsupervised approaches for brain segmentation include coarse white matter/gray matter segmentation [37], [38]. Our work differs from previous approaches in that we do not attempt to recover anatomical regions, but instead simultaneously learn segmentation and latent representations for each partition in a purely data-driven approach.

Prediction from MRI: Machine learning methods for prediction of clinical diagnoses using FreeSurfer based features shows that the choice of machine learning approach may not be as important as the choice of input features [39]. An approach for creating saliency maps, the relevance voxel machine, overlaid on the MRI has been developed specifically targeting volumetric medical imagery [40]. Prediction of Alzheimer's Disease classification using a 3D CNN has been shown to out perform other techniques that utilize multiple imaging modalities [41]. Prediction of subjects' age from structural MRI shows accuracy in the range of ± 10 years [42], [43]. Our approach differs from these in that we first compute a spatially sensitive representation of the MRI data, followed by training a machine learning predictor. This approach allows us to formulate a set of partitions of the brain by which we can compare results across individuals.

III. PROPOSED APPROACH

AutoAtlas is a novel neural network architecture for fully unsupervised partitioning and representation learning of 3D

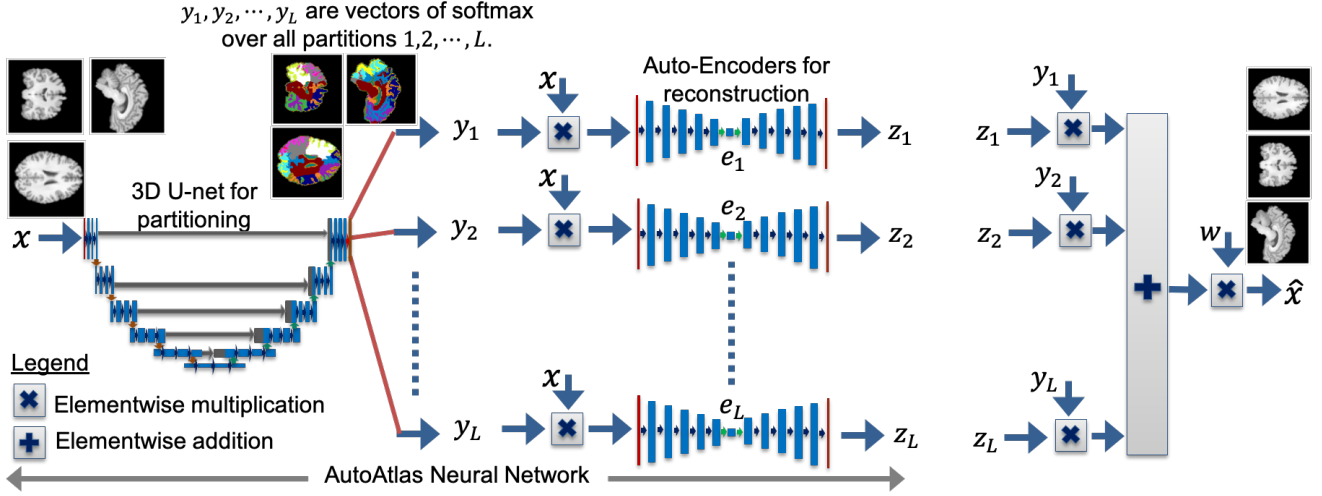


Fig. 1. AutoAtlas consists of a 3D CNN, such as the U-net in this paper, for partitioning the input volume into several partitions each of which is reconstructed using a low-capacity autoencoder. The U-Net is used for 3D multi-label partitioning of the input volume x . The i^{th} autoencoder reconstructs the region within the i^{th} partition. The flow chart to the right is a method to reconstruct the volume \hat{x} from autoencoder reconstructions z_i . However, the reconstructions z_i are directly used in the loss functions (section III-B) instead of \hat{x} .

volumes. It learns to partition the input into multiple regions by consistently recognizing and sparsely encoding the common morphological structure of each region across volumes. The partitions generated by AutoAtlas adapt to variations in morphology and texture from volume to volume.

A. Neural Network Architecture

The architecture of AutoAtlas is shown in Fig. 1. A detailed description of AutoAtlas' neural-network components is presented in Appendix A. A 3D CNN is used to partition the input volume into multiple partitions. We use a 3D U-Net [19], [44] as the 3D CNN for partitioning the MRI brain scans from several subjects. In Fig. 1, the input to the 3D U-Net is the 3D MRI brain volume, which is compactly represented in vector form as $x = [x_1, x_2, \dots, x_N]$ where x_j is the value at the j^{th} input voxel and N is the total number of voxels. The output of the 3D U-Net are vectors of classification probabilities y_1, y_2, \dots, y_L , where L is the total number of partitions and y_i indicates the likelihood of voxels to belong to a particular partition i . Note that $y_i = [y_{i,1}, y_{i,2}, \dots, y_{i,N}]$, where $y_{i,j}$ is the probability that voxel j belongs to partition i . The probabilities $y_{i,j}, 1 \leq i \leq L$ at each voxel j are obtained by a L dimensional softmax at the output of the U-net.

The U-net is followed by multiple low capacity autoencoders where each autoencoder is tasked with the reconstruction of one partition. The i^{th} autoencoder from the top in Fig. 1 strives to accurately reconstruct the input MRI volume x at its output z_i within partition i (where $y_{i,j} \approx 1$). The input to the i^{th} autoencoder is the elementwise vector product of the MRI volume x and the partition probabilities y_i . Each layer of the autoencoder has the same number of channels C_a . At the bottleneck layer where the contracting path ends and the expanding path begins, the total number of activations is also C_a . These activations, henceforth called feature embeddings, represent an encoding of the input volume within the i^{th}

partition (where $y_{i,j} \approx 1$) and are useful for representation learning.

B. Loss Functions

To train AutoAtlas, we minimize the sum of three loss functions each of which serve a unique purpose. The first is Reconstruction Error (RE) loss that is used to measure the quality of autoencoder reconstruction for each partition by comparing the voxel values within the corresponding partition in the input volume. The second is the Neighborhood Label Similarity (NLS) loss that forces neighboring voxels to predict the same label with high confidence. Lastly, we have the Anti-Devouring (AD) loss that imposes a penalty if the number of voxels that belong to a given partition is less than a pre-defined threshold. The AD loss prevents partitions where a few labels devour all the other labels and represent the whole volume.

1) *Reconstruction Error (RE) Loss*: The RE loss is used to ensure that the partitioning is not arbitrary but rather conforming to the distinctive morphological structure in the input brain volumes. It drives the output of every i^{th} autoencoder, z_i , to match the values in the input brain volume, x , within the i^{th} partition. The RE loss penalizes differences between the output of the autoencoder, z_i , and the input volume, x , while weighting the penalty terms by the label probabilities y_i . The penalty terms are also weighted by the foreground mask vector w , where $w_j = 1$ for voxels within the brain and $w_j = 0$ for voxels outside the brain. The weight parameter w_j ensures that AutoAtlas ignores the partitioning of background region with no brain tissue. Thus, the RE loss is given by,

$$L_{RE} = \frac{1}{\bar{w}} \sum_{i=1}^L \sum_{j=1}^N w_j y_{i,j} |x_j - z_{i,j}|^2 \quad (1)$$

where \bar{w} is the total number of voxels within the foreground region given by $\bar{w} = \sum_{j=1}^N w_j$, L is the total number of

partitions, x_j is the value of input volume x at voxel index j , $y_{i,j}$ is the probability of the i^{th} partition label at the j^{th} voxel obtained using the softmax output of the U-net, and $z_{i,j}$ is the j^{th} voxel value at the output of the i^{th} autoencoder that is focused on reconstruction in the i^{th} partition. Given the autoencoder outputs $z_{i,j}$, a reconstruction of voxel j is given by,

$$\hat{x}_j = w_j \sum_{i=1}^L y_{i,j} z_{i,j}. \quad (2)$$

2) *Neighborhood Label Similarity (NLS) Loss*: The NLS loss is used to encourage neighboring voxels to predict the same partition label with high confidence. Two voxels are considered neighbors if they are adjacent in the sense that there is a shared edge or vertex between the voxels. NLS loss not only encourages neighboring voxels to have similar classification probabilities but also forces them to predict only one partition label with high probability.

To guide the formulation of NLS loss, we first define a measure of smoothness for AutoAtlas partitions given by,

$$\sum_{i=1}^L \frac{1}{|\mathcal{N}|} \sum_{k,l \in \mathcal{N}} y_{i,k} y_{i,l}, \quad (3)$$

where L is the total number of partitions, \mathcal{N} is the set of all pairwise indices of voxel neighbors within the foreground region of the brain where $w_j = 1$, and $|\mathcal{N}|$ is the cardinality of the set \mathcal{N} . The term $\frac{1}{|\mathcal{N}|} \sum_{k,l \in \mathcal{N}} y_{i,k} y_{i,l}$ estimates the probability that any two neighboring voxels share the partition label i . Hence, equation (3) estimates the probability that any two neighboring voxels share the same (but any) partition label. Thus, increasing values for equation (3) improves the smoothness of the partitions and also results in high confidence predictions by ensuring

$$\max_i y_{i,j} \approx 1. \quad (4)$$

Suppose the entire brain is assigned a single partition label \hat{i} i.e., $y_{\hat{i},j} \approx 1 \forall j$, then equation (3) will become one.

Our design goal for the NLS loss function is to ensure that equation (3) is maximized. Hence, NLS loss is defined as the negative logarithm of equation (3) and is given by,

$$L_{NLS} = -\log \left(\sum_{i=1}^L \frac{1}{|\mathcal{N}|} \sum_{k,l \in \mathcal{N}} y_{i,k} y_{i,l} \right) \quad (5)$$

By minimizing the NLS loss, we encourage the resulting partitions to be smooth, localized, and contiguous.

3) *Anti-Devouring (AD) Loss*: The AD loss is used to encourage every partition label to be associated with at least a predefined minimum fraction of the total number of voxels in the volume. In the absence of this loss, only a few labels would be chosen to partition the brain by the partitioning CNN, the U-net in Fig. 1, which may lead to large partitions that cannot be accurately reconstructed by the low capacity autoencoders. This in turn leads to insufficient reduction in RE loss and the training converges to a sub-optimal solution. Using AD loss, we are able to drive the partitioning CNN to use all of the

partition labels, thereby presenting each autoencoder with a small sub-region of the brain for encoding and reconstruction.

Our design goal with AD loss is to ensure that every partition satisfies the AD constraint given by,

$$\frac{1}{\bar{w}} \sum_{j=1}^N w_j y_{i,j} \geq u_i, \quad (6)$$

where $0 < u_i \leq 1$ is the desired minimum frequency of occurrence for label i . Note that a voxel j is said to predict a partition label \hat{i} when

$$\hat{i} = \arg \max_i y_{i,j}. \quad (7)$$

In association with the NLS loss that forces $\max_i y_{i,j} \approx 1$, equation (6) ensures that each partition i is predicted by at least u_i fraction of voxels within the brain ($w_j = 1$ defines the interior of the brain).

To ensure that the partitions satisfy equation (6), we minimize the following AD loss,

$$L_{AD} = \frac{1}{L} \sum_{i=1}^L \max \left\{ -\log \left(\frac{1}{u_i \bar{w}} \sum_{j=1}^N w_j y_{i,j} + \epsilon \right), 0 \right\}, \quad (8)$$

where ϵ is a very small value that provides numerical stability. Conversely, if equation (6) is satisfied for i , then the contribution of partition i to the AD loss in equation (8) is zero. In equation (8), the term $\frac{1}{\bar{w}} \sum_{j=1}^N w_j y_{i,j}$ is the average of softmax activations belonging to label i over all voxels within the foreground region where $w_j = 1$. If this term is greater than u_i , then it means that label i has met the desired criteria and does not contribute to the loss. Alternatively, if this term is lower than u_i , then it means label i is under-represented by voxels resulting in positive contribution to the AD loss. The minimum frequency parameter u_i for AD loss is chosen such that it is inversely proportional to the number of labels, L . In particular, we choose $u_i = \frac{c}{L}$, where c is a constant that is close to but less than one. We choose $\epsilon = 10^{-10}$, which ensures that the logarithm in equation (8) is always defined even when $y_{i,j} = 0$ for all j .

4) *Total Loss*: The total loss that is minimized during training is given by the weighted sum of RE, NLS, and AD losses,

$$L_{TOT} = \lambda_{RE} L_{RE} + \lambda_{NLS} L_{NLS} + \lambda_{AD} L_{AD}, \quad (9)$$

where λ_{RE} , λ_{NLS} , and λ_{AD} are the regularization weight hyper-parameters for RE loss, NLS loss, and AD loss respectively. In this paper, λ_{RE} is always chosen to be equal to 1 unless specified otherwise.

C. Representation Learning

In the HCP-YA [9]–[13] dataset, in addition to the MRI scans, several functional and behavioral meta data were collected for each individual subject. AutoAtlas produces several low-dimensional embedding features summarizing each MRI brain volume that are useful to predict such meta data. The dimensionality of the embedding features e_i at the bottleneck layer of each autoencoder is C_a , which in our application is

chosen to be either 4, 8, 16, 32, or 64. Embedding e_i is an encoding of the input volume x multiplied by the classification probabilities y_i as shown in Fig. 11. Importantly, e_i is a C_a dimensional representational encoding of the i^{th} partition. For representation learning, we combine the embeddings from all partitions as,

$$E = [e_1, e_2, \dots, e_L]. \quad (10)$$

The total dimensionality of embeddings in E that includes e_i from all the autoencoders is LC_a , where L is the total number of partitions. Thus, E represents a low-dimensional encoding of the MRI brain volume that is useful to predict other meta data in the HCP-YA dataset.

D. Data and Hyperparameters

We use the Adam optimizer [45] to minimize the total loss function given in equation (9) by jointly optimizing the parameters of the 3D U-net and the autoencoders. For the Adam optimizer, we use a fixed learning rate of 0.0001, momentum parameter of 0.9 for the running average of the gradient, and momentum parameter of 0.999 for the running average of the square of gradient. We use $C_s = 32$ number of channels at the first layer output of U-net shown in Fig. 10. Each input volume is partitioned into $L = 16$ partitions and hence the softmax at the output layer of the U-net in Fig. 10 is over 16 channels. Our choice of $L = 16$ was driven by the limit on the maximum available GPU memory. Larger values for L encourage smaller sized partitions with improved localization and more efficient representation in the feature embeddings, e_i , of autoencoders. The number of channels, C_a , for each autoencoder in Fig. 11 is chosen to be either 4, 8, 16, 32, or 64.

AutoAtlas was trained on a total of 859 MRI volumes for 500 epochs and tested on 215 volumes from the HCP-YA dataset [9]–[14]. All original MRI volumes were down-sampled to a voxel resolution of $2mm$ and zero-padded so that the final size of each volume was $96 \times 96 \times 96$. Next, all volumes are normalized by dividing by the average of the maximum voxel value computed for each volume in the training set. AutoAtlas was then trained using a batch size of 4 on four NVIDIA Tesla V100 GPUs. We used PyTorch [46] machine learning framework for implementing AutoAtlas. We used the same train-test split when predicting meta-data in the HCP-YA dataset from AutoAtlas’ embedding features. After excluding samples with missing meta-data, we had 856 samples for training and 215 samples for testing.

Unless specified otherwise, we always use $\lambda_{RE} = 1$ for the RE loss. While it is possible to get consistent partitions for a wide range of values for the regularization parameters λ_{NLS} and λ_{AD} , incorrect values can still lead to sub-optimal partitions if either of these two regularization parameters are too small. For instance, if $\lambda_{NLS} = 0$, then the U-net is not required by design to produce smooth and contiguous partitions. Alternatively, if $\lambda_{AD} = 0$, then the U-net is not required to use all the available labels and hence it chooses only a small number of labels to partition the whole volume. In this case, due to the large size and complex morphology of each partition, the autoencoder will not be able to encode

and reconstruct it. Thus, consistent partitions are achieved only when both the regularization parameters are set to a sufficiently large value. In our application, we used $\lambda_{RE} = 1$, $\lambda_{NLS} = 0.005$, $\lambda_{AD} = 0.1$, and $u_i = \frac{0.9}{L} = 0.05625$ to train all the AutoAtlas models. The foreground mask w in equation (1) is computed by binary thresholding each MRI volume in the training and testing sets.

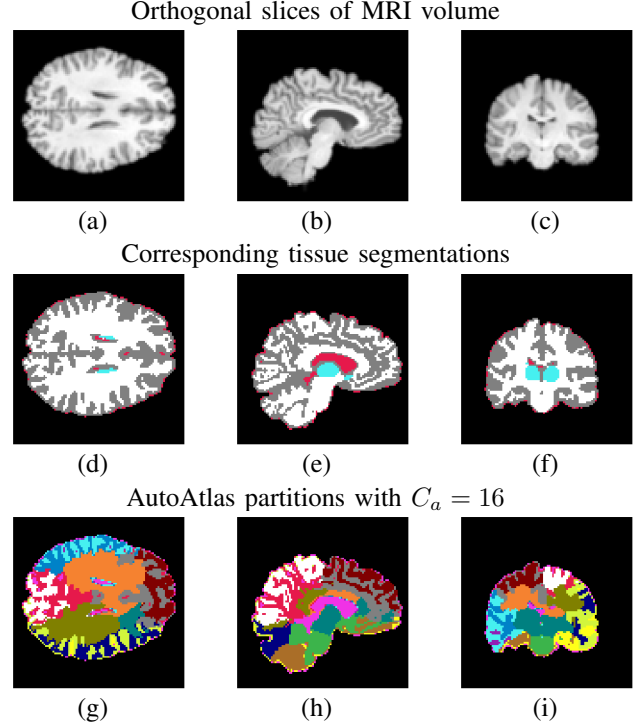


Fig. 2. First row shows MRI image slices along three mutually orthogonal planes for the same subject. Second row shows the corresponding tissue segmentation for images in the first row. Third row shows the resulting partitions using AutoAtlas with $C_a = 16$.

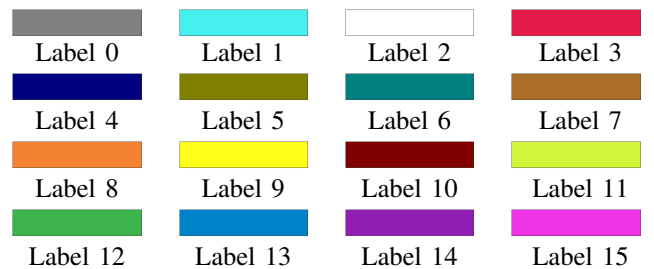


Fig. 3. Legend indicating the color associated with each AutoAtlas label.

IV. RESULTS

In this section, we demonstrate the ability of AutoAtlas to perform 3D unsupervised partitioning of input volume into multiple partitions while producing low dimensional embedding features for each partition that are useful for meta-data prediction. Fig. 2 is a comparison between various tissue types in an MRI volume and the partitions using AutoAtlas. The white, gray, red, and blue colors in the tissue segmentation shown in Fig. 2 (d-f) represent the white matter, gray matter, fluid, and sub-cortical regions respectively. These segmentations were produced using the FAST algorithm [47]. The

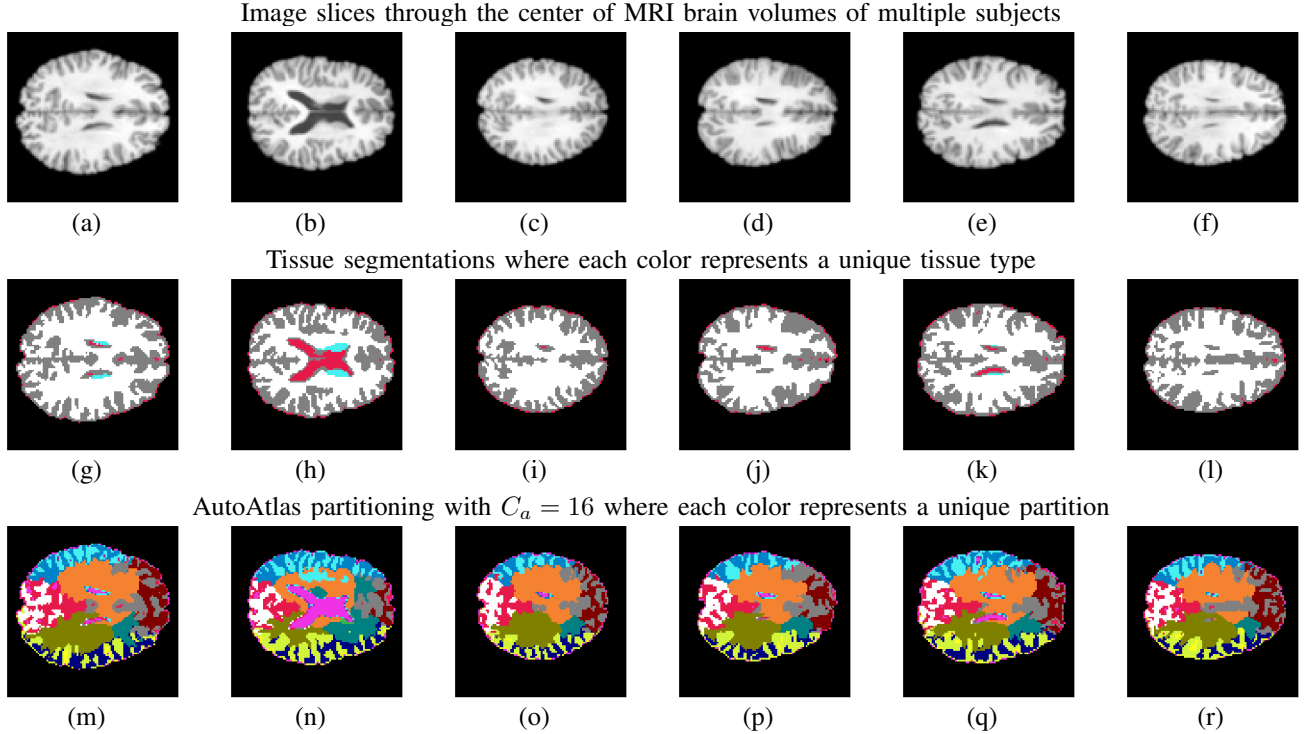


Fig. 4. Comparison of AutoAtlas partitions with tissue segmentations across subjects. First row shows image slices through the center of MRI brain volumes across multiple subjects. Second row shows segmentations of the brain into four different tissue types. Third row shows the partitions generated using AutoAtlas with $C_a = 16$. The images along each column are for the same subject, while the images along a row are for different subjects. The partitioning of AutoAtlas adapt to variations in structure of brain tissue while consistently identifying the same region across subjects.

TABLE I

OVERLAP BETWEEN AUTOATLAS (AA) PARTITIONS AND REGIONS REPRESENTING VARIOUS TISSUE TYPES (TT). THE OVERLAP PERCENTAGE BETWEEN THE i^{th} AUTOATLAS PARTITION (INDICATED BY AA_i) AND j^{th} TISSUE REGION (INDICATED BY TT_j) IS COMPUTED AS THE NUMBER OF VOXELS THAT LIE IN THE INTERSECTION OF THE TWO (AA_i AND TT_j) EXPRESSED AS A PERCENTAGE OF THE TOTAL NUMBER OF VOXELS THAT LIE INSIDE THE BRAIN. THE MEAN (FIRST VALUE) AND STANDARD DEVIATION (SECOND VALUE WITHIN BRACKETS) OF THE OVERLAP PERCENTAGE ACROSS SUBJECTS IS SHOWN FOR EVERY PAIR OF AUTOATLAS PARTITION AND TISSUE REGION. BOLD FONT IS USED TO HIGHLIGHT THE FIELDS FOR WHICH THE MEAN OVERLAP PERCENTAGE IS GREATER THAN ONE. FOR THE TISSUE TYPES, TT_0 IS GRAY MATTER, TT_1 IS SUB-CORTICAL, TT_2 IS WHITE MATTER, AND TT_3 IS FLUID. AUTOATLAS USED AN EMBEDDING SIZE OF $C_a = 16$.

	TT_0	TT_1	TT_2	TT_3
AA_0	5.95 (0.20)	0.00 (0.00)	0.27 (0.04)	0.06 (0.04)
AA_1	5.34 (0.20)	0.02 (0.01)	0.76 (0.10)	0.00 (0.00)
AA_2	1.36 (0.16)	0.00 (0.00)	5.01 (0.23)	0.00 (0.00)
AA_3	5.61 (0.18)	0.00 (0.00)	0.29 (0.08)	0.18 (0.09)
AA_4	3.27 (0.31)	0.00 (0.00)	3.41 (0.34)	0.00 (0.00)
AA_5	0.13 (0.04)	0.00 (0.00)	6.04 (0.23)	0.00 (0.00)
AA_6	0.20 (0.04)	1.33 (0.08)	4.61 (0.19)	0.00 (0.00)
AA_7	4.08 (0.32)	0.00 (0.00)	2.19 (0.36)	0.00 (0.00)
AA_8	0.18 (0.03)	0.37 (0.04)	5.41 (0.15)	0.00 (0.00)
AA_9	5.22 (0.20)	0.07 (0.02)	0.67 (0.12)	0.23 (0.05)
AA_{10}	2.16 (0.22)	0.00 (0.00)	4.02 (0.23)	0.00 (0.00)
AA_{11}	5.80 (0.18)	0.00 (0.00)	0.81 (0.10)	0.00 (0.00)
AA_{12}	1.65 (0.12)	0.54 (0.06)	4.07 (0.21)	0.00 (0.00)
AA_{13}	1.51 (0.13)	0.01 (0.01)	4.88 (0.22)	0.00 (0.00)
AA_{14}	4.70 (0.47)	0.00 (0.00)	1.51 (0.47)	0.05 (0.02)
AA_{15}	1.90 (0.28)	0.01 (0.01)	0.00 (0.01)	4.11 (0.48)

AutoAtlas labels associated with each color of the resulting partitions in Fig. 2 (g-i) is shown in Fig. 3. By comparing

the AutoAtlas partitions in Fig. 2 (g-i) with the tissue regions in Fig. 2 (d-f), we can see that the boundaries of AutoAtlas partitions conform to the tissue boundaries. Fig. 4 demonstrates the consistency of AutoAtlas partitions across various subjects. Each distinct color marks a unique partition that is consistently recognized in the brain scans across multiple subjects. Importantly, the structure of each partition varies to account for the morphological changes in brain tissue across subjects. The autoencoder plays an important role to achieve this behavior by sparsely encoding and decoding the partition associated with each label. The images in Fig. 2 and Fig. 4 are for subjects from the test set using an AutoAtlas model with $C_a = 16$.

Table I quantifies the consistency of brain partitioning across various subjects by presenting the mean and standard deviation of the percentage of overlap between AutoAtlas partitions and various tissue types. Each row in Table I corresponds to one AutoAtlas partition and each column corresponds to a tissue type (white matter, sub-cortical region, gray matter, or fluid). The amount of overlap between AutoAtlas partitions and tissue types is quantified as a percentage of the total brain volume¹. The mean values of overlap percentage in Table I indicate that each AutoAtlas partition overlaps significantly with only one or two tissue types. When compared to the mean, the relatively low values for standard deviation of the overlap percentage, shown in Table I, demonstrate that the percentage overlap is similar valued across subjects. This demonstrates

¹Total brain volume is the number of voxels that contain brain tissue and excludes the background voxels.

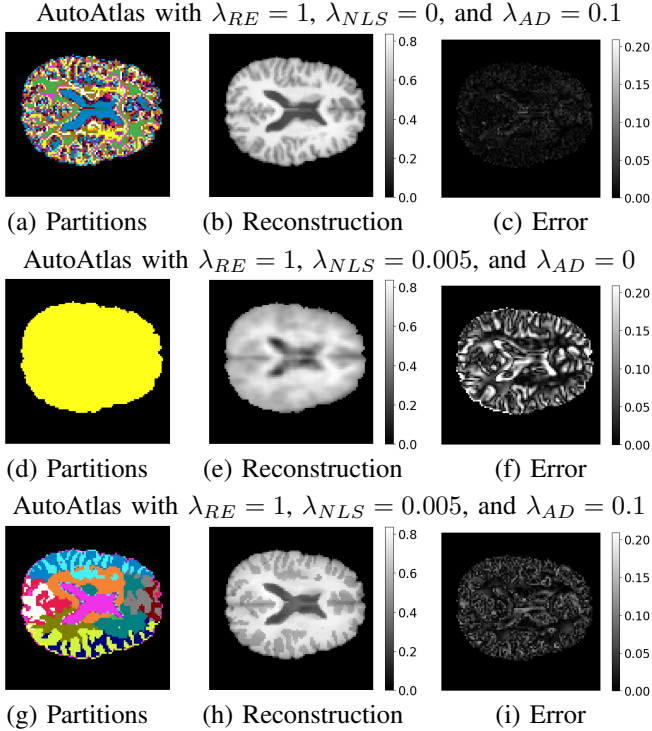


Fig. 5. Ablation study of the NLS and AD losses (equations (5) and (8)) by analyzing the partitioning and reconstruction performance of AutoAtlas. Each color in (a,d,g) represents a unique partition. The reconstruction in (b,e,h) is computed using the flow-chart shown on the right side of Fig. 1. The reconstruction error in (c,f,i) is computed as the absolute value of the difference between the reconstruction and the ground-truth MRI. By comparing (a) and (g), we see that the NLS loss is responsible for producing smooth and contiguous partitions. From (e,h) and (f,i), we see that incorporation of the AD loss produces a more accurate reconstruction by encouraging multiple partitions that each have their own representation.

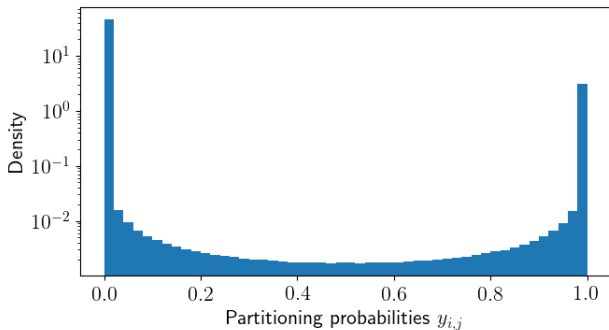


Fig. 6. 50 bin normalized histogram of the partitioning probabilities $y_{i,j}$ for all the volumes in the test set. Note that the y -axis is logarithm scaled. We can see that $y_{i,j}$ is predominantly either 0 or 1.

that each partition produced by AutoAtlas consistently learns to recognize and encode the same brain tissue.

The partitions in Fig. 2 and Fig. 4 are a direct result of the interplay between the loss functions in equations (1), (5), and (8). An ablation study demonstrating the utility of the NLS loss and AD loss in AutoAtlas partitioning is shown in Fig. 5. The results in Fig. 5 and Fig. 4 (b,h,n) are for the same subject. The reconstructions in Fig. 5 (b,e,h) are obtained by computing $\hat{x} = w \sum_{i=1}^L z_i y_i$ as shown in Fig. 1. The reconstruction error in Fig. 5 (c,f,i) is computed as $|\hat{x} - x|$, where x is the ground-

truth MRI that is input to AutoAtlas. While Fig. 5 (a-c) and Fig. 5 (d-f) are for two different AutoAtlas models trained in the absence of the NLS loss ($\lambda_{NLS} = 0$) and the AD loss ($\lambda_{AD} = 0$) respectively, Fig. 5 (g-i) is for an AutoAtlas model that used all the three losses. By comparing Fig. 5 (a-c) with Fig. 5 (g-i), we can see that the NLS loss is necessary to get smooth and contiguous partitions while still being able to accurately reconstruct the input MRI volume. By comparing Fig. 5 (d-f) with Fig. 5 (g-i), we can see that the AD loss contributes to efficient partitioning of input volume into several representable partitions that are accurately reconstructed by the autoencoders. Note that $y_{i,j} \approx 1$ if voxel j is within the i^{th} partition and $y_{i,j} \approx 0$ otherwise (Fig. 6). The purpose of the mask w is to ignore the partitioning and reconstruction in the background where there is no brain tissue.

For representation learning, we compare prediction performances obtained by feeding the embedding features, E in equation (10), as input to machine learners such as ridge regression, nearest neighbor regression, support vector machine (SVM), and multi-layer perceptron (MLP). As a baseline, we also report performance scores for predictors trained using 201 structural features extracted by Freesurfer [17]. We evaluated prediction of all meta-data related to motor skills with the names *Strength-Unadj*, *Strength-AgeAdj*, *Endurance-Unadj*, *Endurance-AgeAdj*, *Dexterity-Unadj*, *Dexterity-AgeAdj*, and *GaitSpeed-Comp*. However, we noticed that both Freesurfer features and AutoAtlas features were only predictive for the meta-data, *Strength-Unadj* and *Strength-AgeAdj*. *Strength-Unadj* is a measure of the grip strength of each hand and *Strength-AgeAdj* measures grip strength while correcting for variations due to age.

Table II compares the predictive performance of AutoAtlas' embedding features and Freesurfer features as measured using the coefficient of determination² (R^2) and mean absolute error³ metrics. We used the python based machine learning package *scikit-learn* [48] to train and test all the regressors in Tables II, III, and IV. The regularization for each predictor was tuned using an automated grid search strategy and 3-fold cross validation on the training data. More details regarding the chosen hyper-parameters for the predictors in Table II are presented in Appendix B. The prediction performance using AutoAtlas features generally improve with increasing values for the embedding size C_a as shown in Table II. This behavior can be attributed to the improved information retention when using larger embedding sizes. However, the performance stagnates beyond $C_a = 16$ since increasing C_a beyond 16 does not further improve the encoded information content in the embedding.

In Table III, we quantify the importance of each individual embedding feature vector e_i (section III-C), which encodes the information within partition i , when predicting *Strength-Unadj* and *Strength-AgeAdj*. The importance score for a partition i is computed as the percentage increase in mean absolute error after randomly permuting⁴ the embedding features e_i .

²The R^2 score is one for a regressor that always predicts correctly.

³Mean of the absolute value differences between prediction and ground-truth

⁴Average score is reported over 10 randomized permutations.

TABLE II

PERFORMANCE COMPARISON BETWEEN AUTOATLAS AND FREESURFER FEATURE BASED REGRESSORS. LEGEND: FS - FREESURFER FEATURES, AAK - AUTOATLAS FEATURES WITH $C_a = K$ EMBEDDING SIZE FOR EACH AUTOENCODER, LIN - RIDGE REGRESSION, NNBOR - NEAREST NEIGHBOR, SVM - SUPPORT VECTOR MACHINE, MLP - MULTI-LAYER PERCEPTRON. AUTOATLAS' PREDICTION PERFORMANCE IMPROVES WITH INCREASING C_a UNTIL $C_a = 16$. PERFORMANCE IS MEASURED USING THE COEFFICIENT OF DETERMINATION, (R^2), (LARGER IS BETTER) AND THE MEAN ABSOLUTE ERROR (SMALLER IS BETTER).

	Prediction of meta-data <i>Strength-Unadj</i>								Prediction of meta-data <i>Strength-AgeAdj</i>							
	Coefficient of determination (R^2)				Mean Absolute Error				Coefficient of determination (R^2)				Mean Absolute Error			
	Lin	NNbor	SVM	MLP	Lin	NNbor	SVM	MLP	Lin	NNbor	SVM	MLP	Lin	NNbor	SVM	MLP
FS	0.343	0.323	0.387	0.383	7.02	7.03	6.83	6.75	0.350	0.324	0.385	0.384	13.14	13.11	12.18	12.51
AA4	0.371	0.318	0.378	0.392	6.96	7.30	6.94	6.82	0.378	0.322	0.380	0.393	12.68	13.45	12.56	12.55
AA8	0.402	0.382	0.421	0.397	6.77	6.84	6.73	6.63	0.405	0.374	0.418	0.408	12.44	12.67	12.16	12.17
AA16	0.451	0.384	0.449	0.451	6.53	6.87	6.58	6.51	0.456	0.379	0.420	0.423	12.13	12.86	12.07	12.13
AA32	0.435	0.335	0.439	0.454	6.64	7.18	6.55	6.47	0.442	0.335	0.398	0.457	12.25	13.32	12.26	11.71
AA64	0.440	0.370	0.430	0.446	6.58	7.10	6.61	6.49	0.448	0.375	0.421	0.453	12.01	12.87	12.09	11.92

TABLE III

IMPORTANCE SCORE FOR EACH 16 DIMENSIONAL EMBEDDING FEATURE e_i (SECTION III-C) OBTAINED USING AUTOATLAS WITH $C_a = 16$. FOR EACH PARTITION i , THE IMPORTANCE SCORE IS COMPUTED AS THE PERCENTAGE INCREASE IN THE MEAN ABSOLUTE ERROR AFTER PERMUTATION OF THE EMBEDDING FEATURES e_i AMONG ALL THE SUBJECTS. FROM THE SCORES, WE CAN SEE THAT A FEW PARTITIONS ARE CONSISTENTLY DETERMINED TO BE IMPORTANT BY MULTIPLE REGRESSORS.

(a) Prediction of meta-data *Strength-Unadj*

Optim	f_0	f_1	f_2	f_3	f_4	f_5	f_6	f_7	f_8	f_9	f_{10}	f_{11}	f_{12}	f_{13}	f_{14}	f_{15}
Lin	1.33	0.74	3.57	1.24	2.15	1.39	3.09	2.58	0.81	2.41	6.20	-0.01	2.06	3.57	6.18	-0.34
SVM	0.75	0.11	3.41	1.13	0.91	-1.27	1.01	3.46	0.28	-1.05	1.61	-0.17	-0.34	2.69	3.28	0.63
NNbor	0.94	1.43	1.52	0.11	1.07	0.96	0.75	-0.10	1.22	-0.22	0.99	0.17	0.49	1.27	1.02	1.35
MLP	4.04	1.66	6.58	2.00	2.18	0.33	0.59	3.88	3.12	1.89	4.46	0.05	2.33	0.97	5.44	0.35

(b) Prediction of meta-data *Strength-AgeAdj*

Optim	f_0	f_1	f_2	f_3	f_4	f_5	f_6	f_7	f_8	f_9	f_{10}	f_{11}	f_{12}	f_{13}	f_{14}	f_{15}
Lin	1.18	0.88	4.37	1.54	2.21	2.40	3.39	3.98	1.08	3.33	5.14	0.11	2.33	3.38	5.61	-0.15
SVM	1.60	0.81	6.43	1.57	1.18	-0.55	1.11	3.67	0.88	-0.55	2.30	0.08	-0.01	1.69	3.08	0.06
NNbor	0.87	1.06	1.54	-0.02	0.87	0.47	0.65	0.07	0.79	-0.29	0.96	-0.11	0.35	0.79	0.69	0.74
MLP	2.08	0.56	7.58	0.47	1.70	1.14	0.42	4.74	0.15	0.67	2.43	0.07	0.82	0.46	3.05	-0.06

TABLE IV

ABLATION STUDY OF AUTOATLAS LOSSES BY COMPARING THE PREDICTION PERFORMANCE DURING REGRESSION OF *Strength-Unadj*. THE BEST PERFORMANCE IS OBTAINED ALONG THE LAST ROW WHERE ALL THE THREE LOSSES ARE IN USE ($\lambda_{AD} \neq 0$, $\lambda_{NLS} \neq 0$, AND $\lambda_{RE} \neq 0$). IN THE ABSENCE OF AD LOSS ($\lambda_{AD} = 0$), WE SEE THAT AUTOATLAS ONLY USES ONE LABEL TO REPRESENT THE WHOLE BRAIN RESULTING IN INCREASED ROOT MEAN SQUARED ERROR (RMSE) FOR THE RECONSTRUCTION. IN THE ABSENCE OF NLS LOSS ($\lambda_{NLS} = 0$), EVEN THOUGH THE RMSE IS THE LOWEST, THE NON-SMOOTH PARTITIONS (FIG. 5(A)) RESULT IN LOWER PREDICTION PERFORMANCE THAN THE LAST ROW. WITHOUT THE RE LOSS ($\lambda_{RE} = 0$), THE PREDICTION PERFORMANCE SUFFERS DUE TO LOSS OF INFORMATION IN THE EMBEDDINGS e_i .

λ_{RE}	λ_{NLS}	λ_{AD}	RMSE	Regions	Coefficient of determination (R^2)				Mean absolute error			
					Lin	SVM	NNbor	MLP	Lin	SVM	NNbor	MLP
0.0	0.005	0.1	0.60	12	0.37	0.35	0.35	-0.01	7.12	7.18	7.26	9.23
1.0	0.0	0.1	0.02	16	0.38	0.41	0.39	0.33	7.03	6.76	6.93	7.20
1.0	0.005	0.0	0.09	1	0.38	0.38	0.35	-0.00	6.90	6.92	7.00	9.21
1.0	0.005	0.1	0.04	16	0.45	0.45	0.38	0.45	6.53	6.58	6.87	6.51

Permutation refers to the process of randomly shuffling the vector of embedding features among all the subjects in the test set. In Fig. 7, we overlay the importance score for e_i (Table III) over partition i in order to associate the partition-specific importance scores with the corresponding location of each partition in the MRI scan. From Fig. 7, we can see that partitions located along the cortical surface seem to be more important than the interior regions when predicting *Strength-Unadj* and *Strength-AgeAdj*. We also include supporting multimedia files in the form of MP4 videos to visualize the MRI volumes, AutoAtlas partitions, and the overlay of importance scores on the partitions.

Table IV is an ablation study of the RE (equation (1)), NLS (equation (5)), and AD (equation (8)) losses that compares the representation learning performance. The 5th column (titled

“Regions”) in Table IV shows that both AD loss and RE loss play a pivotal role in ensuring that all 16 labels are utilized to represent the volume. From 4th column (titled “RMSE”) of Table IV, we see that while the constraints imposed by the NLS loss tend to increase the reconstruction error, AD and RE losses strive to reduce it. Irrespective of the reconstruction error, the simultaneous use of the RE, NLS, and AD losses results in the best representation learning performance.

To guide our selection of regularization hyper-parameters, λ_{NLS} and λ_{AD} in equation (9), we plot various metrics that quantify the nature of AutoAtlas partitions and reconstruction on the training set as a function of either λ_{NLS} or λ_{AD} in Fig. 8. Due to underfitting of our AutoAtlas models, we chose to perform hyper-parameter tuning using the training set instead of a separate validation set. For the purpose of hyper-

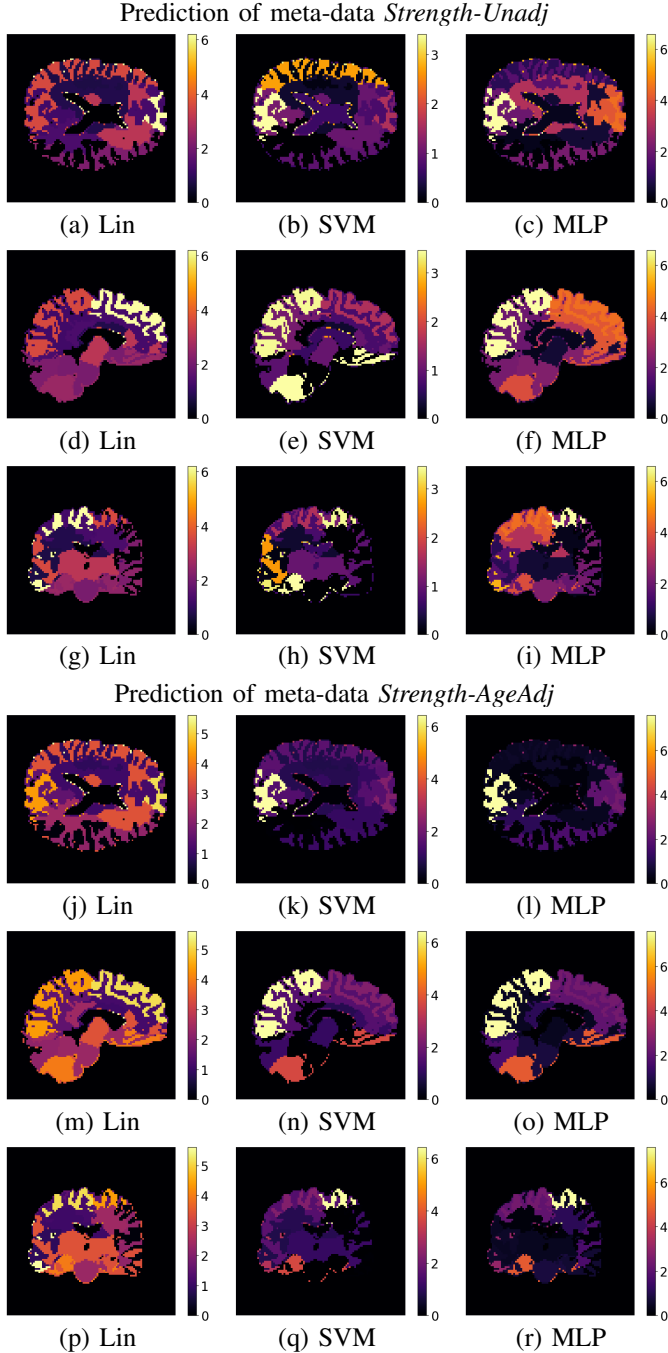


Fig. 7. Overlay map of the importance scores on the brain volume of an individual subject. Partitions located in the cortical surface seem to be more important than the interior partitions when predicting both *Strength-Unadj* and *Strength-AgeAdj*.

parameter tuning, we only trained AutoAtlas for 200 epochs. Each plot in Fig. 8 perform a parameter sweep along the horizontal axis over either λ_{AD} or λ_{NLS} in logarithmic steps while assuming constant values for the other regularization hyper-parameters. Fig. 8 (a, f) plot the number of partitions that satisfy the AD constraint shown in equation (6) along the vertical axis. Fig. 8 (b, g) plot the number of partitions whose voxel count is more than 5.625%⁵ of the total number of voxels

⁵Given by $u_i \times 100 = 5.625\%$, where u_i is defined in equation (6).

within the brain (a voxel’s partition membership is defined in equation (7)). Fig. 8 (c, h) plot the root mean squared error (RMSE) between the reconstruction, \hat{x} as defined in equation (2), and the ground-truth input volume x (Fig. 1). Fig. 8 (d, i) show the percentage of voxels that satisfy the constraint $\max_i y_{i,j} \geq 0.99$, which indicates high-confidence predictions (i.e., satisfy equation (4)). Lastly, Fig. 8 (e, j) plot a measure of the smoothness of AutoAtlas partitions as defined in equation (3). Note that all plots in Fig. 8 plot the average value over all volumes in the training set along the vertical axis.

For hyper-parameter tuning, we first empirically choose an appropriate λ_{AD} while setting $\lambda_{RE} = 1$ and $\lambda_{NLS} = 0$ in equation (9). In Fig. 8 (a-e), we plot metrics that quantify the partitioning performance and reconstruction fidelity as a function of λ_{AD} when $\lambda_{NLS} = 0.0$. From Fig. 8 (a), we can see that λ_{AD} must be chosen to have a sufficiently large value in order to ensure that the AD constraint is satisfied. However, the number of partitions with significant voxel count shown in Fig. 8 (b) does not follow a predictable pattern due to the absence of NLS loss. From Fig. 8 (c), we observe that the RMSE measure appears to be inversely correlated to the number of partitions in Fig. 8 (b). As λ_{AD} is increased, we also observe a decrease in both the percentage of voxels with high-confidence predictions in Fig. 8 (d) and the measure of partition smoothness in Fig. 8 (e). Guided by Fig. 8 (a-e), we choose $\lambda_{AD} = 0.1$ since it is the lowest value that satisfies the AD constraint in Fig. 8 (a).

To choose an appropriate value for λ_{NLS} , we examine Fig. 8 (f-j) that analyze the partitioning performance and reconstruction fidelity as a function of λ_{NLS} when $\lambda_{RE} = 1$ and $\lambda_{AD} = 0.1$. From Fig. 8 (f, g), we observe that large values for λ_{NLS} invalidate the AD constraint by forcing the whole brain to be represented by only one partition. Unlike Fig. 8 (a, b), Fig. 8 (f) and Fig. 8 (g) follow a similar behavior due to the presence of NLS loss. For large values of λ_{NLS} that result in a single partition for the whole brain (Fig. 8 (f, g)), the RMSE in Fig. 8 (h) is also high since a single low-capacity autoencoder is tasked with reconstruction of the whole brain. As λ_{NLS} is increased, we also observe an increase in the percentage of voxels with high-confidence predictions in Fig. 8 (i) and the measure of smoothness in Fig. 8 (j). We choose a value of $\lambda_{NLS} = 0.005$ that provides an acceptable trade-off of low RMSE, smooth partitions, and a large number of voxels with high-confidence predictions. While we chose to avoid further tuning of λ_{AD} , such a tuning may be valuable in a different application.

To evaluate the robustness of AutoAtlas and its applicability to a broad range of datasets, we tested our AutoAtlas model (the model used in Fig. 4 and Fig. 2) on the MRI of a subject diagnosed with Traumatic Brain Injury (TBI) [49]. Note that AutoAtlas was trained solely on MRIs of healthy subjects in the HCP-YA dataset [9]–[14]. Hence, testing on an MRI with TBI represents a drastic change from the distribution of samples used to train AutoAtlas. A comparison between various orthogonal slices through the MRI volume and its AutoAtlas partitions is shown in Fig. 9. In spite of TBI, the performance of AutoAtlas in Fig. 9 is consistent with Fig. 4, Fig. 2, and Fig. 3. This behavior demonstrates the robust nature

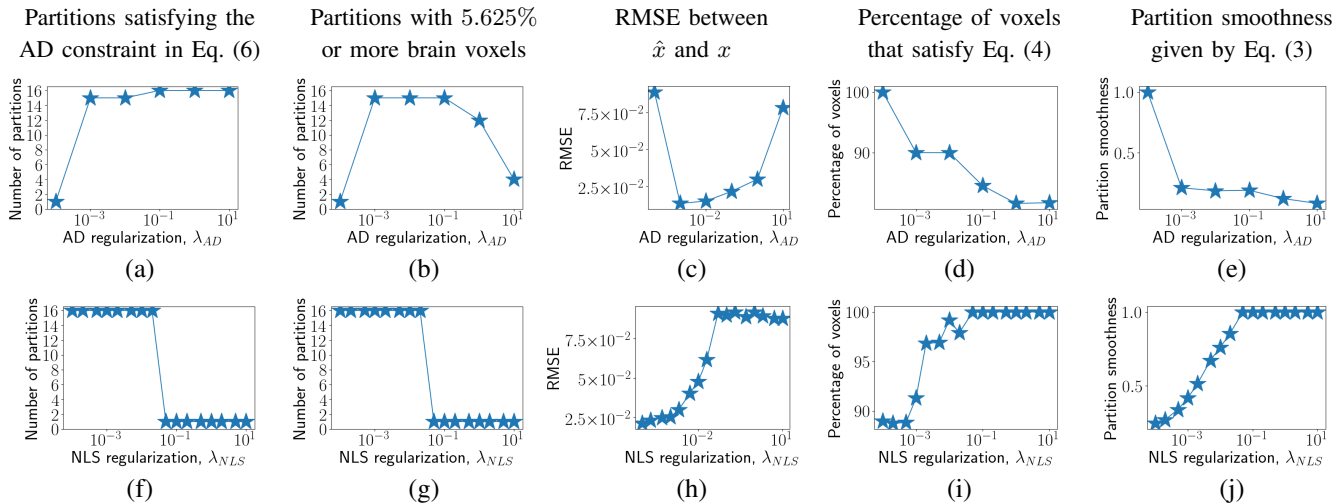


Fig. 8. Partitioning performance and reconstruction fidelity as a function of the regularization hyper-parameters in equation (9). In the 1st column, we plot the number of partitions that satisfy the AD constraint in equation (6). In the 2nd column, we plot the number of partitions that occupy more than 5.625% of all voxels inside the brain, where the partition associated with each voxel is given by equation (7). In the 3rd column, we plot the RMSE between the reconstruction, \hat{x} , and the ground-truth volume x (Fig. 1). In the 4th column, we plot the percentage of voxels that predict only one partition label with high confidence (equation (4)). In the 5th column, we plot a measure of the smoothness of the AutoAtlas partitions as quantified by equation (3). In the first row, we plot as a function of the AD regularization hyper-parameter λ_{AD} when $\lambda_{NLS} = 0$. In the second row, we plot as a function of the NLS regularization hyper-parameter λ_{NLS} when $\lambda_{AD} = 0.1$. Note that Eq. is an abbreviation for equation.

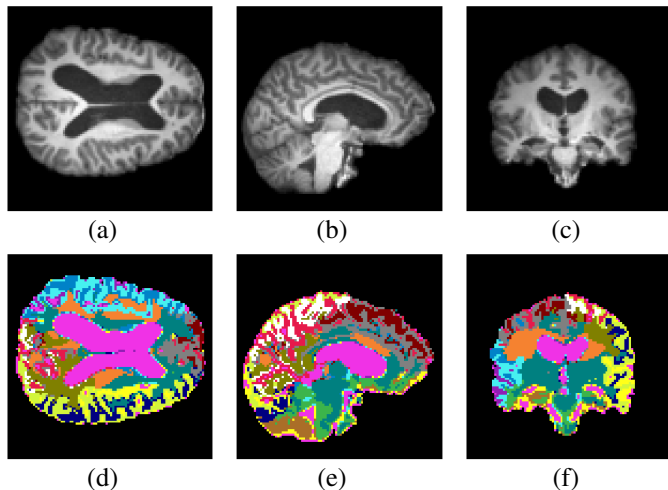


Fig. 9. Testing of AutoAtlas on an MRI of a subject with TBI. (a,b,c) show perpendicularly oriented slices through the center of the MRI scan. (d,e,f) show the partitions generated using AutoAtlas. In the slice shown in (d), the ventricles appear enlarged when compared to the MRIs of healthy subjects in Fig. 4.

of AutoAtlas even when evaluated on a radically different dataset than the one used for training.

Our approach is also applicable to the analysis of volumes containing pathological features. Depending on the underlying nature of the pathology, we may observe different characteristics for the partitions and the embeddings. For subjects with traumatic brain injury, we may see partitions that are either entirely missing or significantly different from normative cases. Alternatively, Alzheimer’s Disease may result in volumetric changes to the partitions due to reduced gray matter volume. Since the embedding features (equation (10)) and the partitions’ shapes and sizes are directly impacted by

the changes described above, we expect that the AutoAtlas representation may be useful in prediction and localization of pathology.

V. ACKNOWLEDGMENT

LLNL-JRNL-815848 and LLNL-VIDEO-816094. This work was performed under the auspices of the U.S. Department of Energy by Lawrence Livermore National Laboratory (LLNL) under Contract DE-AC52-07NA27344. This work has been supported in part by grants from the DOE Office of Science’s Advanced Computing Science Research (Grant #KJ0403020). Data was provided by the Human Connectome Project (HCP), WU-Minn Consortium (Principal Investigators: David Van Essen and Kamil Ugurbil; 1U54MH091657) funded by the 16 NIH Institutes and Centers that support the NIH Blueprint for Neuroscience Research; and by the McDonnell Center for Systems Neuroscience at Washington University.

APPENDIX A NEURAL NETWORK ARCHITECTURE

The architecture of U-net used in this paper is shown in Fig. 10. It consists of a contracting path where the 3D size is progressively halved in each dimension followed by an expansive path where the 3D size is progressively doubled. The contracting path consists of multiple downsampling stages where each stage has three 3D convolutional layers each of which is followed by a ReLU activation layer. The first convolutional layer at each stage doubles the number of channels when compared to its input. The output of every stage is downsampled by a factor of 2 in each spatial dimension using a max-pool layer. The number of channels at the output of the first convolutional layer is denoted by the parameter C_s . At the end of the contracting path, there is an expansive

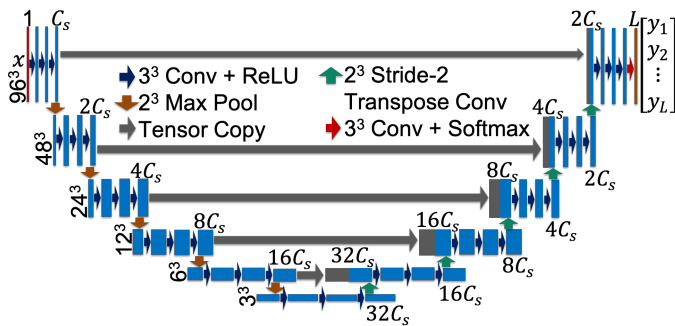


Fig. 10. A 3D U-Net is used to partition the input volume into L partitions. Each rectangle represents a tensor. The number of channels is indicated above or below the tensor. The spatial size is indicated to the left of the tensor.

path with multiple stages each of which consists of three sets of convolutional and ReLU layers. The input for each stage in the expansive path is the concatenation of the output of the previous stage and the same sized output from the earlier contracting path. The output of each stage is up-sampled by a factor of 2 along each spatial dimension using a 3D transposed convolutional layer with a stride of 2. This layer also halves the number of channels when compared to its input. The last layer of the U-net is a softmax over L number of channels for each voxel. The softmax computes the classification probability vector for each voxel.

Similar to the U-net, our autoencoder architecture also has a contracting path followed by an expansive path. However, unlike U-net, there are no cross-connections from the contracting path to the expansive path. This ensures that all information has to flow through the bottleneck layer at the center of the autoencoder in between the contracting and expansive paths. At each stage in the contracting path, the 3D size is halved in each spatial dimension using a convolutional layer with a stride of 2. In the expansive path, each stage consists of a transposed convolutional layer with a stride of 2 to double the 3D size in each spatial dimension. Every convolutional and transposed convolution layers are followed by a ReLU activation layer except at the last stage that produces the reconstruction z_i . The number of channels is fixed at a value of C_a at the output of each convolutional layer in the autoencoder. At the bottleneck layer that is in between the contracting and expansive paths, a fully connected layer (FC) transforms the output of the last contracting stage into a vector of size C_a . Another FC layer transforms this vector into a multi-dimensional tensor with C_a number of channels that serves as input to the first stage in the expansive path.

APPENDIX B

REPRESENTATION LEARNING PARAMETERS

All the machine learning approaches used to predict the meta data *Strength-Unadj* and *Strength-AgeAdj* in Tables II and III were implemented using the python package *scikit-learn*⁶ version 0.22.1. Before training and testing, the class *sklearn.preprocessing.StandardScaler* was used to normalize

⁶<https://scikit-learn.org/>

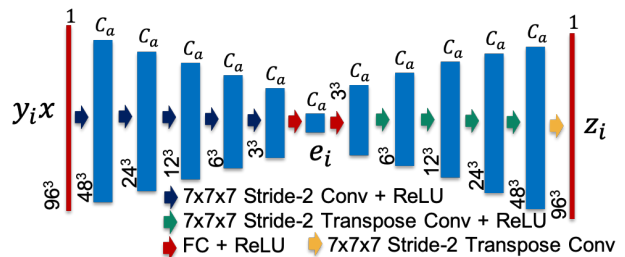


Fig. 11. 3D autoencoder for reconstruction of voxels contained within partition i . e_i is a vector denoting the embedding features in the bottleneck layer. Each rectangle represents a tensor. The number of channels is indicated above the tensor. The spatial size is indicated to the left of the tensor.

all features by mean subtraction and dividing by the standard deviation. The mean and standard deviation parameters were computed from the training set.

The class *sklearn.linear_model.Ridge* was used to train the linear ridge regressor (tag “Lin” in Tables II and III). The optimal regularization parameter, α , was chosen to maximize the R^2 score using 3-fold cross-validation by searching over a grid of 44 values, which were logarithmically spaced from a starting value of 10^{-5} up to a maximum value that was strictly less than 10^6 . We used the *lsqr* solver and default values for all other parameters.

The class *sklearn.neighbors.KNeighborsRegressor* was used to train the nearest neighbor regressor (tag “NNbor” in Tables II and III). The number of neighbors parameter, $n_neighbors$, was chosen to maximize the R^2 score using 3-fold cross-validation and grid-search over grid values of 1, 2, 3, 4, 5, 6, 8, 9, 11, 13, 16, 19, 22, 26, 32, 38, 45, 53, 64, 76, 90, 107, 128, 152, 181, and 215.

The class *sklearn.svm.SVR* was used to perform support vector regression (tag “SVM” in Tables II and III). The regularization parameter C was chosen to maximize the R^2 score using 3-fold cross-validation by searching over a grid of 44 values, which were logarithmically spaced from a starting value of 10^{-5} up to a maximum value that was strictly less than 10^6 . The kernel coefficient γ was chosen to be inversely proportional to the number of features. All other hyper-parameters were left at their respective default values.

The class *sklearn.neural_network.MLPRegressor* was used to perform regression using a multi-layer perceptron (MLP) architecture (tag “MLP” in Tables II and III). MLP used two hidden layers of sizes 4 (first hidden layer) and 2 (second hidden layer) for all prediction tasks irrespective of the number of features. We used the *lbfgs* solver and a maximum number of 10^5 iterations. The L2 regularization parameter α was chosen to maximize the R^2 score using 3-fold cross-validation by searching over a grid of 44 values, which were logarithmically spaced from a starting value of 10^{-5} up to a maximum value that was strictly less than 10^6 .

REFERENCES

- [1] Y. Bengio, A. Courville, and P. Vincent, “Representation learning: a review and new perspectives,” *IEEE Trans. Pattern Anal. Mach. Intell.*, vol. 35, no. 8, pp. 1798–1828, Aug. 2013.

- [2] K. Fukunaga, *Introduction to Statistical Pattern Recognition*. Academic Press, Oct. 2013.
- [3] J. Shawe-Taylor and N. Cristianini, *Kernel Methods for Pattern Analysis*. Cambridge University Press, Jun. 2004.
- [4] I. Goodfellow, Y. Bengio, A. Courville, and Y. Bengio, *Deep learning*. MIT press Cambridge, 2016, vol. 1.
- [5] X. Chen, Y. Duan, R. Houthoofd, J. Schulman, I. Sutskever, and P. Abbeel, “InfoGAN: Interpretable representation learning by information maximizing generative adversarial nets,” in *Advances in Neural Information Processing Systems* 29, D. D. Lee, M. Sugiyama, U. V. Luxburg, I. Guyon, and R. Garnett, Eds. Curran Associates, Inc., 2016, pp. 2172–2180.
- [6] L. Tran, X. Yin, and X. Liu, “Disentangled representation learning gan for pose-invariant face recognition,” in *Proceedings of the IEEE conference on computer vision and pattern recognition*. openaccess.thecvf.com, 2017, pp. 1415–1424.
- [7] S. B. Eickhoff, B. T. T. Yeo, and S. Genon, “Imaging-based parcellations of the human brain,” *Nat. Rev. Neurosci.*, vol. 19, no. 11, pp. 672–686, Nov. 2018.
- [8] D. S. Bassett and O. Sporns, “Network neuroscience,” *Nat. Neurosci.*, vol. 20, no. 3, pp. 353–364, Feb. 2017.
- [9] D. C. Van Essen, S. M. Smith, D. M. Barch, T. E. J. Behrens, E. Yacoub, K. Ugurbil, and WU-Minn HCP Consortium, “The WU-Minn human connectome project: an overview,” *Neuroimage*, vol. 80, pp. 62–79, Oct. 2013.
- [10] M. F. Glasser *et al.*, “The human connectome project’s neuroimaging approach,” *Nat. Neurosci.*, vol. 19, no. 9, pp. 1175–1187, Aug. 2016.
- [11] S. M. Smith *et al.*, “Resting-state fMRI in the human connectome project,” *Neuroimage*, vol. 80, pp. 144–168, Oct. 2013.
- [12] D. M. Barch *et al.*, “Function in the human connectome: task-fMRI and individual differences in behavior,” *Neuroimage*, vol. 80, pp. 169–189, Oct. 2013.
- [13] D. C. Van Essen *et al.*, “The human connectome project: a data acquisition perspective,” *Neuroimage*, vol. 62, no. 4, pp. 2222–2231, Oct. 2012.
- [14] M. F. Glasser *et al.*, “The minimal preprocessing pipelines for the human connectome project,” *Neuroimage*, vol. 80, pp. 105–124, 2013.
- [15] E. Landhuis, “Neuroscience: Big brain, big data,” *Nature*, vol. 541, no. 7638, pp. 559–561, Jan. 2017.
- [16] S. Lemm, B. Blankertz, T. Dickhaus, and K.-R. Müller, “Introduction to machine learning for brain imaging,” *Neuroimage*, vol. 56, no. 2, pp. 387–399, May 2011.
- [17] R. S. Desikan *et al.*, “An automated labeling system for subdividing the human cerebral cortex on MRI scans into gyral based regions of interest,” *Neuroimage*, vol. 31, no. 3, pp. 968–980, Jul. 2006.
- [18] J. Long, E. Shelhamer, and T. Darrell, “Fully convolutional networks for semantic segmentation,” in *Proceedings of the IEEE conference on computer vision and pattern recognition*. cv-foundation.org, 2015, pp. 3431–3440.
- [19] O. Ronneberger, P. Fischer, and T. Brox, “U-net: Convolutional networks for biomedical image segmentation,” in *International Conference on Medical image computing and computer-assisted intervention*. Springer, 2015, pp. 234–241.
- [20] Ö. Çiçek, A. Abdulkadir, S. S. Lienkamp, T. Brox, and O. Ronneberger, “3D U-Net: Learning dense volumetric segmentation from sparse annotation,” Jun. 2016.
- [21] I. Aganj, M. G. Harisinghani, R. Weissleder, and B. Fischl, “Unsupervised medical image segmentation based on the local center of mass,” *Sci. Rep.*, vol. 8, no. 1, p. 13012, Aug. 2018.
- [22] K. Tang, A. Joulin, L. Li, and L. Fei-Fei, “Co-localization in Real-World images,” in *2014 IEEE Conference on Computer Vision and Pattern Recognition*, Jun. 2014, pp. 1464–1471.
- [23] M. Cho, S. Kwak, C. Schmid, and J. Ponce, “Unsupervised object discovery and localization in the wild: Part-based matching with bottom-up region proposals,” in *Proceedings of the IEEE Conference on Computer Vision and Pattern Recognition*, 2015, pp. 1201–1210.
- [24] D. Novotny, D. Larlus, and A. Vedaldi, “AnchorNet: A weakly supervised network to learn geometry-sensitive features for semantic matching,” Apr. 2017.
- [25] A. Kanazawa, D. W. Jacobs, and M. Chandraker, “WarpNet: Weakly supervised matching for Single-View reconstruction,” in *2016 IEEE Conference on Computer Vision and Pattern Recognition (CVPR)*, Jun. 2016, pp. 3253–3261.
- [26] J. Thewlis, H. Bilen, and A. Vedaldi, “Unsupervised learning of object landmarks by factorized spatial embeddings,” in *2017 IEEE International Conference on Computer Vision (ICCV)*, Oct. 2017, pp. 3229–3238.
- [27] Y. Zhang, Y. Guo, Y. Jin, Y. Luo, Z. He, and H. Lee, “Unsupervised discovery of object landmarks as structural representations,” in *Proceedings of the IEEE Conference on Computer Vision and Pattern Recognition*. openaccess.thecvf.com, 2018, pp. 2694–2703.
- [28] S. Arslan, S. I. Ktena, A. Makropoulos, E. C. Robinson, D. Rueckert, and S. Parisot, “Human brain mapping: A systematic comparison of parcellation methods for the human cerebral cortex,” *Neuroimage*, vol. 170, pp. 5–30, Apr. 2018.
- [29] M. F. Glasser *et al.*, “A multi-modal parcellation of human cerebral cortex,” *Nature*, vol. 536, no. 7615, pp. 171–178, Aug. 2016.
- [30] C. Destrieux, B. Fischl, A. Dale, and E. Halgren, “Automatic parcellation of human cortical gyri and sulci using standard anatomical nomenclature,” *Neuroimage*, vol. 53, no. 1, pp. 1–15, Oct. 2010.
- [31] A. de Brebisson and G. Montana, “Deep neural networks for anatomical brain segmentation,” in *Proceedings of the IEEE Conference on Computer Vision and Pattern Recognition Workshops*. cv-foundation.org, 2015, pp. 20–28.
- [32] B. Fischl *et al.*, “Whole brain segmentation: automated labeling of neuroanatomical structures in the human brain,” *Neuron*, vol. 33, no. 3, pp. 341–355, Jan. 2002.
- [33] H. Chen, Q. Dou, L. Yu, J. Qin, and P.-A. Heng, “VoxResNet: Deep voxelwise residual networks for brain segmentation from 3D MR images,” *Neuroimage*, vol. 170, pp. 446–455, Apr. 2018.
- [34] B. Patenaude, S. M. Smith, D. N. Kennedy, and M. Jenkinson, “A bayesian model of shape and appearance for subcortical brain segmentation,” *Neuroimage*, vol. 56, no. 3, pp. 907–922, Jun. 2011.
- [35] M. Havaei *et al.*, “Brain tumor segmentation with deep neural networks,” *Med. Image Anal.*, vol. 35, pp. 18–31, Jan. 2017.
- [36] G. P. Mazzara, R. P. Velthuisen, J. L. Pearlman, H. M. Greenberg, and H. Wagner, “Brain tumor target volume determination for radiation treatment planning through automated MRI segmentation,” *Int. J. Radiat. Oncol. Biol. Phys.*, vol. 59, no. 1, pp. 300–312, May 2004.
- [37] D. Rivest-Hénault and M. Chériet, “Unsupervised MRI segmentation of brain tissues using a local linear model and level set,” *Magn. Reson. Imaging*, vol. 29, no. 2, pp. 243–259, Feb. 2011.
- [38] Y. Kong, Y. Deng, and Q. Dai, “Discriminative clustering and feature selection for brain MRI segmentation,” *IEEE Signal Process. Lett.*, vol. 22, no. 5, pp. 573–577, May 2015.
- [39] M. R. Sabuncu, E. Konukoglu, and Alzheimer’s Disease Neuroimaging Initiative, “Clinical prediction from structural brain MRI scans: a large-scale empirical study,” *Neuroinformatics*, vol. 13, no. 1, pp. 31–46, Jan. 2015.
- [40] M. R. Sabuncu, K. Van Leemput, and Alzheimer’s Disease Neuroimaging Initiative, “The relevance voxel machine (RVoxM): a self-tuning bayesian model for informative image-based prediction,” *IEEE Trans. Med. Imaging*, vol. 31, no. 12, pp. 2290–2306, Dec. 2012.
- [41] E. Hosseini-Asl, R. Keynton, and A. El-Baz, “Alzheimer’s disease diagnostics by adaptation of 3D convolutional network,” in *2016 IEEE International Conference on Image Processing (ICIP)*. IEEE, Sep. 2016, pp. 126–130.
- [42] K. Franke, G. Ziegler, S. Klöppel, C. Gaser, and Alzheimer’s Disease Neuroimaging Initiative, “Estimating the age of healthy subjects from t1-weighted MRI scans using kernel methods: exploring the influence of various parameters,” *Neuroimage*, vol. 50, no. 3, pp. 883–892, Apr. 2010.
- [43] K. Franke, E. Luders, A. May, M. Wilke, and C. Gaser, “Brain maturation: predicting individual BrainAGE in children and adolescents using structural MRI,” *Neuroimage*, vol. 63, no. 3, pp. 1305–1312, Nov. 2012.
- [44] Ö. Çiçek, A. Abdulkadir, S. S. Lienkamp, T. Brox, and O. Ronneberger, “3d U-net: learning dense volumetric segmentation from sparse annotation,” in *International conference on medical image computing and computer-assisted intervention*. Springer, 2016, pp. 424–432.
- [45] D. P. Kingma and J. Ba, “Adam: A method for stochastic optimization,” *arXiv preprint arXiv:1412.6980*, 2014.
- [46] A. Paszke *et al.*, “Automatic differentiation in PyTorch,” in *NIPS Autodiff Workshop*, 2017.
- [47] Y. Zhang, M. Brady, and S. Smith, “Segmentation of brain MR images through a hidden markov random field model and the expectation-maximization algorithm,” *IEEE Transactions on Medical Imaging*, vol. 20, no. 1, pp. 45–57, 2001.
- [48] F. Pedregosa *et al.*, “Scikit-learn: Machine learning in Python,” *Journal of Machine Learning Research*, vol. 12, pp. 2825–2830, 2011.
- [49] A. Roy *et al.*, “The evolution of cost-efficiency in neural networks during recovery from traumatic brain injury,” *PLOS ONE*, vol. 12, no. 4, pp. 1–26, 04 2017.